Revised manuscript (clean version) Click here to view linked References

The nanoscale explanation of metal cations differences in enhancing the Fe(III) coagulation performance

Bingqian Yang[a,b], Peng Zhou[a,b], Long Tian[a,b], Nigel Graham[c], Guibai Li[d], Zhaoyang Su [a*], and Wenzheng Yu[a*]

[a] State Key Laboratory of Environmental Aquatic Chemistry, Key Laboratory of Drinking Water Science and Technology, Research Center for Eco-Environmental Sciences, Chinese Academy of Sciences, Beijing 100085, People's Republic of China (wzyu@rcees.ac.cn)

[b] College of Resources and Environment, University of Chinese Academy of Sciences (UCAS), Beijing 100049, China

[c] Department of Civil and Environmental Engineering, Imperial College London, South Kensington Campus, London SW7 2AZ, United Kingdom (n.graham@imperial.ac.uk)

[d] State Key Laboratory of Urban Water Resource and Environment (SKLUWRE), Harbin Institute of Technology, 73 Huanghe Road, Nangang District, Harbin 150090, PR China

ABSTRACT

Coagulation is a widely applied and important process for water treatment, and the development of improved coagulation reagents continues to be a practical objective. However, mechanisms guiding the development of composite coagulants remain insufficiently understood. In addressing this deficiency, this study has investigated the enhancement of conventional Fe(III) coagulation by composite coagulants that incorporate an additional metal salt (Me: Ca^{2+}, Al^{3+}, Ti^{4+}, Zr^{4+}), focusing on the mechanistic roles that Me constituents play in Fe-based coagulation. The effectiveness of composite coagulants was assessed through floc size and the removal of organics and phosphates. Results demonstrated that Me constituents enhance coagulation performances to varying extents, with Al^{3+} and Zr^{4+} showing the most significant improvements. FT-ICR MS analysis at the molecular scale reveals that additional Me facilitates the removal of humic acid, hydrophobic macromolecules, and highly aromatic organics containing polycarboxyl and secondary carbon structures. EXAFS results indicate that co-hydrolysis of Fe^{3+} with Me disrupts the formation of conventional ferrihydrite at the nanoscale of flocs and promotes the development of Fe-phosphate clusters. Me effectively reduces the corner- and edge-sharing coordination between FeO_6 octahedra within clusters, resulting in a more dispersed arrangement of FeO_6 polymers with available binding sites for the PO_4 tetrahedron. The shortened Fe-P bond indicates that Me promotes a more compact link between FeO_6 octahedra and PO_4 tetrahedra. By revealing how cations in composite coagulants change the nanoscale structure of Fe flocs to affect macroscopic coagulation, this study enhances the understanding of metal ion interactions during co-hydrolysis and co-precipitation in natural systems.

Keywords: Coagulation; Composite coagulants; Phosphate; Fe; EXAFS; Natural organic matter

1. Introduction

The coagulation process, which removes pollutants through the hydrolysis of metal ions (Me) and the aggregation of floc particles, has been an effective water treatment method for centuries and is widely used in various applications (Dayarathne et al., 2021; Duan and Gregory, 2003; Matilainen et al., 2010). Simultaneously, the development of coagulants has remained a significant area of research. Conventional coagulants, such as those based on iron (Fe) and aluminum (Al), have proven to be cost-effective in removing particles, organic matter, and harmful ions (Liu et al., 2024b; Xu et al., 2024a). Other coagulants, such as titanium (Ti) and zirconium (Zr) salts, have emerged as promising candidates for future applications due to their higher charge densities (Gan et al., 2019; Jarvis et al., 2012; Wang et al., 2016; Zhao et al., 2016). The practice of selecting multiple metal ion coagulants for specific water treatment challenges, to reduce chemical consumption, lower sludge production, and improve operational efficiency, has become increasingly common. Composite coagulants, formed by combining different Me, offer advantages such as a broader hydrolysis pH range and enhanced charge neutralization (Zhao et al., 2016). Several composite coagulants, including Al-Fe, Al-Ti, and Al-Zr, have been shown in numerous studies to outperform single-component coagulants (Liu et al., 2022; Liu et al., 2023; Xue et al., 2024; Zhuang et al., 2021). With a deeper understanding of the co-hydrolysis mechanism of multiple Me, more cost-effective, adaptable, and efficient composite coagulants can be developed and optimized to address emerging challenges in municipal and industrial water treatment. However, despite these advances, there is still no unified theory that fully explains the differences in the coagulation behaviour of composite coagulants. Additionally, the hydrolysis mechanisms of these composite coagulants require further detailed investigation (Wang et al., 2020).

Phosphate is a common inorganic anion associated with environmental issues such as algal blooms and eutrophication, which inhibits the hydrolysis of Me during the early nucleation process, leading to the formation of flocs with smaller and more complex amorphous structures (Anderson et al., 2002; Correll, 1998). Previous studies have demonstrated that this inhibition can be overcome by optimizing the type of metal ion additives,

thereby improving coagulation efficiency in drinking water and wastewater treatment (Smotraiev et al., 2022; Wang et al., 2023b). Thus, further systematic research is required to elucidate how different metal salts interact with phosphate and influence phosphate removal during coagulation.

The coagulation process of inorganic Me is typically divided into ion hydrolysis, cluster formation, cluster aggregation, and particle aggregation (Fig. 1a) (Das, 2018; LaGrow et al., 2019). The hydrolysis and precipitation of Me in the environment are often accompanied by complexation with other ions and organics (Hiemstra, 2018; Kraal et al., 2022). The coagulation process of composite coagulants can be viewed as a co-hydrolysis and co-precipitation process of multiple Me in aqueous environments (Shi et al., 2018; Yang et al., 2023a). Previous studies have shown that the hydrolysis of Me can be affected by other ions during the cluster formation stage, altering the nanoscale structure of flocs and thus affecting the subsequent coagulation process (Wang et al., 2023a). Due to their poor crystallinity and disorder, the resulting hydrolysates exhibit large and intricate complexity. Studies have shown that these products can be composed of colloids, short-range-ordered minerals (dozens of atoms arranged within a few nanometers), clusters (dimers or trimers), or polymer chains (Henneberry et al., 2012; Mertens et al., 2016; Tamrat et al., 2019). For example, the hydrolysis of Fe(III) coagulants results in oligomer clusters formed by edge- or corner-sharing FeO_6 octahedra chains, which have not yet reached the polymerization level of ferrihydrite (Chen et al., 2014; Son et al., 2020). The aggregation of these clusters and the subsequent growth of polymer chains are crucial in determining the formation of flocs at the nanoscale (Li et al., 2018). Water quality factors, such as pH and the presence of background organic substances and ions, can affect the coagulation process through the aggregation of these clusters (Gentile et al., 2018; Lartiges et al., 2019; Yang et al., 2023a). Owing to current limitations in analytical methods, it remains a challenge to study the short-range ordered structure and local coordination environment of hydrolysis clusters at the molecular scale (Frenkel et al., 2001; Rehr and Albers, 2000; Son et al., 2020).

In this study, four previously used or studied Me salts (Ca^{2+}, Al^{3+}, Ti^{4+}, Zr^{4+}) were each combined with Fe(III) salts to form different composite coagulants. These coagulants were employed to treat various representative phosphorus-rich water bodies, aiming to elucidate their mechanisms for enhancing the efficacy of conventional (single cation) Fe(III) coagulants. Specifically, this research has quantified the improvements of different Me on conventional Fe(III) coagulation across multiple dimensions: the hydrodynamic behaviour of flocs, the efficiency of phosphate removal, and the selective extraction of organics with diverse structures. Furthermore, a detailed analysis of floc structures was conducted, emphasizing the chemical forms and bond coordination of Fe oxyhydroxide in flocs generated by various composite coagulants. This investigation contributes to a deeper understanding of the mechanisms governing the coagulation and hydrolysis processes of metal salts and provides valuable insights for the development and targeted application of innovative composite coagulants.

2. Materials and Methods

2.1 Chemicals and Reagents

The coagulants employed in this experiment were all prepared using metal sulfates. $Fe_2(SO_4)_3$ (Sigma, USA) alone was used to represent the conventional Fe(III) coagulant, and other Me (Ca^{2+}, Al^{3+}, Ti^{4+}, Zr^{4+}) were used with Fe^{3+} to synthesize Fe-Me composite coagulants (Ding et al., 2024; Liu et al., 2024a). A corresponding quantity of concentrated Me sulfate solution was added dropwise to a concentrated solution of $Fe_2(SO_4)_3$ to prepare a composite coagulant, achieving molar concentration ratios of Me to Fe^{3+} ions of 1:6, 1:3, 1:2, and 2:3. During the mixing process, the solution was stirred rapidly while a small amount of H_2SO_4 was added dropwise to maintain the pH of the coagulant solution at 1.5, preventing Me precipitation and ensuring the pH of the different composite coagulant stock solutions remained consistent.

To assess the universality of coagulation strategies across varied scenarios, we employed water samples containing waterborne and terrestrial organics to represent aquatic and terrestrial water bodies, respectively. The raw water with waterborne organics (AT) was collected from Beijing Olympic Park, a typical reclaimed lake water source (Guo et al., 2017; Su et al., 2021). The raw water with terrestrial organics (HA) was prepared by diluting humic acid powder (Sigma, USA) in deionized water supplemented with buffer (5mM sodium bicarbonate). Given the inherent pH buffering capacity of natural water, no additional buffers were added to the AT water to avoid interference (Li et al., 2023b; Zhang et al., 2022). Adjustments to the concentrations of added humic and hydrochloric acid were made to ensure consistent total organic carbon (TOC) and pH levels between these raw water samples. All experiments employed the same batch of water samples, which were filtered through a 0.45 μm microfiltration membrane to eliminate microorganisms and insoluble impurities. A certain amount (0.048 mmol/L) of Na_2HPO_4 was added to the raw water to achieve a 1.5 mg P/L phosphorus concentration, reflecting a typical level found in eutrophic surface water and effluent following primary biofilter treatment (Douterelo et al., 2020; Li et al., 2023a; Rezania et al., 2022; Zhang et al., 2024). Physicochemical parameters that could affect coagulation,

including dissolved oxygen content (3-5 mg/L), temperature (20-24 ºC), and pH (7.0-7.5), were monitored before and after the experiments to ensure consistent experimental conditions, as summarized in Table 1.

Table 1. The properties of the raw water used in the experiments

Physical/chemical indicators	**AT**	**HA**
pH	7.2 (±0.3)	7.2 (±0.1)
Dissolved oxygen (mg/L)	5.27 (±0.2)	5.43 (±0.5)
TOC (mgC/L)	5.57 (± 0.22)	5.12 (± 0.54)
UV_{254} (a.u./cm)	0.049	0.210
UV_{280} (a.u./cm)	0.037	0.181
Ca^{2+} concentration (mg/L)	3.56	0
P concentration (mg/L)	1.5 (± 0.2)	1.5 (± 0.2)
Conductivity (μ S/cm)	1055.9 (± 8.5)	2238.3 (± 6.5)
Temperature (ºC)	23 (± 2)	23 (± 2)
F^- concentration (mg/L)	0.37	0.1
Silicate concentration (mg/L)	0.15	0.08
Mg^{2+} concentration (mg/L)	0.41	0.26

2.2 Coagulation experiment and floc detection method

The coagulant concentrations reported in this study reflect the actual amounts added to the raw water, with the dosage of Fe(III) controlled at 0.15 mM to explore the effects of different Me types and dosages on enhanced coagulation. 1 L of phosphorus-containing raw water was treated using a Flocculator apparatus, following a mixing-growth-floc breakage-regrowth protocol: The system was initially stirred at 200 rpm for 30 s to mix the raw water and coagulant. The stirring rate was then reduced to 50 rpm for 30 min to allow floc growth and aggregation. After that, the stirring rate was again increased to 200 rpm for 30 seconds to break the formed flocs and then adjusted back to 50 rpm to observe their regrowth. To ensure the reliability of the data, coagulation experiments were conducted in triplicate under all conditions.

During coagulation, macroscopic floc size was monitored indirectly in real-time using an optical photometric dispersion analyzer (PDA3000, Rank Brothers, UK). When floc growth reached equilibrium, the microscopic size and surface zeta potential of particles were measured with a Zeta Potential Analyzer (Malvern ZS90, UK) to calculate their interaction forces based on the Derjaguin-Landau-Verwey-Overbeek (DLVO) theory; the details are shown in the SI (Text S1).

Residual phosphate in solution was determined at various time intervals using an inductively coupled plasma mass spectrometer (ICP-MS, Perkin, USA) to elucidate the kinetics of phosphate removal by different coagulants; the details are shown in the SI (Text S7).

After coagulation and 10 min of sedimentation, the supernatant was filtered using a 0.45 μm microfiltration membrane for DOM characterization, and the settled flocs were collected and freeze-dried for subsequent analysis.

2.3 DOM Analytical Methods

The following methods were employed to quantify DOM changes after coagulation: fluorescent substance data were obtained using a fluorescence spectrophotometer (Hitachi, Japan) and analyzed in MATLAB to obtain the composition information; details are shown in

the SI (Text S2-3). The DOM (UV-sensitive substances) was analyzed by a HPLC system (Waters, USA) with a Security Guard™ column (Phenomenex) via size exclusion chromatography (SEC) to obtain the molecular weight distribution; the detected organics were classified into high molecular weight organics (HMW), medium molecular weight organics (MMW), low molecular weight organics (LMW), and very low molecular weight organics (VLMW), based on their molecular weights. The discrimination rules are outlined in the SI (Text S4). UV-visible spectrophotometry (Shimadzu, Japan) and a TOC analyzer (Shimadzu, Japan) were used to determine solution absorbance and TOC concentration. These data were evaluated using principal component analysis (PCA) to identify key factors influenced by the composite coagulants.

Coagulated water samples underwent solid phase extraction (SPE) for desalination and concentration, and were analyzed by Fourier transform ion cyclotron resonance mass spectrometry (FT-ICR MS, USA) with a Bruker SolariX FT-ICR mass spectrometer (15 T) to examine molecular formula differences in DOM removed by different coagulants. The methodologies for molecular formula analysis are described in the SI (Text S5).

2.4 Density Functional Theory (DFT) Calculation Methods

Three well-proved complex forms between phosphate and the FeO_6 dimer were modeled using Gaussian 16 for cluster density functional theory (DFT) calculations.(Collins et al., 2016; Kubicki et al., 2012; Pincus et al., 2020). The differences in bond dissociation energy, surface electrostatic potential (ESP), the highest occupied molecular orbital (HOMO), and the lowest unoccupied molecular orbital (LUMO) were subsequently analyzed. Details are provided in the SI (Text S6) (Lu, 2024; Yoshizawa, 2012).

2.5 Characterization and Analysis for Flocs

Flocs in sediments were analyzed using X-ray photoelectron spectroscopy (XPS, ULVAC, Japan), Fourier Transform infrared spectroscopy (FTIR, Thermo, USA), and a high-resolution transmission electron microscope (HRTEM, Tecnai, USA) equipped with energy-dispersive X-

ray spectrometry (EDS) to obtain structure information.

Synchrotron Fe K-edge EXAFS data were collected on the BL14W1 beamline at the Shanghai Synchrotron Radiation Facility (SSRF). Details regarding the beamline instrumentation, data collection settings, and analysis methods for EXAFS experiments are provided in the SI (Text S8).

3. Results and discussion

3.1 Improvement in floc growth by Fe^{3+}-Me composite coagulants

The value of Ksp, calculated by Visual Minteq, indicates that within the studied pH range, the selected Me ions exhibited a significant propensity for hydrolysis and precipitate formation (SI, Fig. S1)(Cao et al., 2002; Unsworth et al., 2006). This suggests a high likelihood of coprecipitation between Me ions and Fe^{3+} in composite coagulants, thereby enhancing coagulation. Fig. 1b illustrates that the coagulation performance of Fe^{3+} salts alone was suboptimal under the experimental conditions, primarily due to the inhibitory effects of phosphates and organics on floc growth. Phosphate, functioning as an anion, impedes coagulation by forming smaller clusters with Fe^{3+} during the initial nucleation phase and preventing particles from agglomerating by increasing the negative charge on their surface in the subsequent floc growth stage (Lartiges et al., 2019). Introducing different composite coagulants alleviated these inhibitory effects to varying extents: as added Me ions increased, the maximum equilibrium floc size improved by 5.62% (Ca^{2+}), 11.09% (Al^{3+}), 11.72% (Ti^{4+}), and 9.46% (Zr^{4+}), respectively. Notably, Fe-Al and Fe-Zr composite coagulants accelerate floc growth and facilitate earlier equilibrium. Compared to Zr^{4+} and Al^{3+}, the weaker hydrolysis of Ti^{4+} means that more time is required to reach equilibrium in floc growth (SI, Fig. S1). Moreover, the resilience of flocs produced by composite coagulants was significantly enhanced during the breakage and regrowth phases, suggesting that the introduction of Me, particularly Ti^{4+}, increases the proportion of active groups (-OH_2 and -OH) on the floc surface, enhancing their elastic recovery properties and facilitating floc reaggregation (Liu et al., 2024c).

Following coagulation, the supernatant was analyzed to assess phosphate removal by the various coagulants. The application of composite coagulants led to significant improvements in phosphate removal compared to using Fe coagulant alone (only a 52.8% reduction in phosphate levels by Fe^{3+}), with the order of effectiveness being $Al^{3+} > Zr^{4+} > Ti^{4+} > Ca^{2+}$ (Fig. 1c). The addition of Al^{3+}, Zr^{4+}, and Ti^{4+} notably enhanced the flocculation index, and reduced the phosphate concentration in the treated water to below 0.2 mg/L (>87%), which meets the Chinese National requirements of grade III drinking water sources (2002). The results underscore the effectiveness of employing multi-metal composite coagulants in overcoming the inhibitory effects of phosphate on floc growth, thereby enhancing overall removal efficiency. A similar trend was observed in HA water, where the larger molecular weight of terrestrial organic matter posed a stronger challenge to coagulation. Only the Fe-Al and Fe-Zr composite coagulants successfully achieved the desired phosphate removal targets (SI, Fig. S2).

The zeta potential of the coagulation system utilizing Fe coagulant alone was found to be -32.36 mV. The introduction of additional cations significantly reduced the zeta potential of flocs (Fig. 1d) by increasing the positive charge on their surfaces (Xu et al., 2024b). Furthermore, the incorporation of Me ions effectively increased the particle size of floc monomers (Fig. 1e). Electrostatic repulsion and van-der-Waals forces between particles formed by different coagulants were calculated to estimate the energy barrier governing floc agglomeration (SI, Fig. S3). DLVO results revealed that the use of composite coagulants (except Ca^{2+}) effectively neutralized the energy barrier between particles, facilitating the agglomeration of particles that would otherwise repel each other in the case of using conventional Fe^{3+} coagulant alone (Fig. 1f) (Hotze et al., 2010).

Figure 1

3.2 DOM removal improved by Fe^{3+}-Me composite coagulants

Fig. 2a-d illustrates changes in fluorescent compositions of different water samples after coagulation. PARAFAC analysis identified three major components in these samples (SI, Fig.

S4 and Table S1). Results indicate that phosphate limits the effectiveness of Fe(III) coagulation in removing hydrophilic NOM from surface water, particularly affecting C1(fulvic-like) and C2 (humic-like) components. However, the Fe-Me composite coagulants enhanced the removal of all components, with significant improvements observed in removing C1 and C2. Among the coagulants tested, Fe-Al exhibited the highest performance, followed by Fe-Zr, while Fe-Ca was most effective in enhancing C3 (protein-like) removal. For HA, which contains a higher concentration of hydrophobic DOM, Fe-Al and Fe-Zr significantly improved the removal of C2 components, while the effects of Ca^{2+} and Ti^{4+} were less pronounced due to their higher solubility products (Ksp), which led to complex formation with DOM and incomplete hydrolysis. In both water bodies, it was observed that as the concentration of Al^{3+} and Zr^{4+} increased, more humified and terrestrial organics were removed, suggesting that this phenomenon was applicable widely to different water types. Consequently, the proportion of microbial-derived organic matter in the water increased after coagulation, and indices such as biological index (BIX), freshness index (FRI), and fluorescence index (FLUI) also increased (SI, Fig. S5). In contrast, the increase in the concentration of Ca^{2+} and Ti^{4+} did not significantly affect the fluorescence index of the water after coagulation, suggesting that their removal on organics has insignificant selectivity. Regional integration results demonstrated the order of fluorescence removal ability as follows: Fe-Al > Fe-Zr > Fe-Ti > Fe-Ca (SI, Fig. S6).

Compared to surface water, HA water contains a higher concentration of macromolecular substances exceeding 10 kDa. Thus, the coagulation process is more effective at removing UV-sensitive substances from HA water than from AT water. (Fig. 2e). Increasing the concentration of Me effectively enhances the removal of organic molecules across various molecular weight ranges through coagulation. SEC analysis indicates that the improvements in removing soluble organics by composite coagulants are primarily concentrated in the high- and medium-molecular-weight range of substances. Among tested coagulants, Fe-Al demonstrated the most substantial enhancement, achieving an overall removal rate of UV-sensitive substance of 50.03% in AT water and 92.15% in HA water with a 0.1 mM Me dosage, followed by Fe-Ti and Fe-Zr (Fig. 2f-g and S7). However, for very low molecular weight (<5 kDa) substances, particularly

hydrophilic DOM, altering the type of coagulant still failed to achieve effective removal. UV_{254} and UV_{280} serve as key indicators in water treatment practice, representing the aromatic hydrocarbon and double bond content of NOM (Chen et al., 2018). Our findings reveal that increasing the concentration of Me ions in composite coagulants can effectively enhance the removal of these water quality indicators (SI, Fig. S8-9). All four composite coagulants significantly improved the removal of aromatic and double-bond structures in HA water. However, in AT water, only the Fe-Al and Fe-Zr showed notable improvements.

Indicators such as MMW, BIX, FRI, and UV_{254}, primarily contribute to the first principal component (PC1) in PCA, which shows that they have similar behavior during the coagulation. The second principal component (PC2) is mainly influenced by indicators with minor changes after coagulation, including HIX, C3, RI, RII, and VLMW, explaining 23.6% of the total variance (Fig 2j). The similarity in confidence ellipses indicates that Ca^{2+} and Ti^{4+} ions exert comparable effects in enhancing the NOM removal efficiency of Fe coagulant, whereas adding Al^{3+} or Zr^{4+} exhibits a stronger overall capacity for DOM removal. In summary, increasing the dosage of Me enhances NOM removal efficiency regardless of whether the water contains waterborne or terrestrial NOM. Notably, terrestrial humic macromolecules, which contain double-bond and aromatic structures, are more readily removed. However, the effect of different Me on improving NOM removal efficiency varied significantly. The clearer separation of variables in Fig. S10, based on differences in raw water, indicated that the intrinsic NOM quality of the raw water is a key factor influencing the effectiveness of coagulation in removing organic matter.

Figure 2

3.3 Molecular variations of DOM improved by Fe^{3+}-Me composite coagulants

Extracted DOM from AT water treated with different coagulants can help elucidate the mechanisms by which composite coagulants enhance DOM removal at the molecular scale (Fig. 3: blue and violet indicated the further removed substances by Fe-Al and Fe-Zr than

conventional Fe^{3+} coagulant, respectively; gray represents the stubborn part that still cannot be removed). The results show that DOM is primarily concentrated within a H/C ratio range of 0.4 to 2.0 and an O/C ratio range of 0.1 to 0.95, with lignin (approximately 75%) and proteins (about 12%) being dominant components, consistent with the EEM results. Composite coagulants predominantly enhance the removal of lignin identified by CHNO, CHOS, and CHNOS formulas, condensed aromatics with a high O/C ratio, tannins characterized by CHO and CHOS formulas, and proteins. Furthermore, Fe-Al exhibited a stronger removal capability for condensed aromatics and lignin than Fe-Zr, while Fe-Zr was more effective in removing lipids and carbohydrates. Nonetheless, lignin and proteins that were composed solely of CHO, remained predominant components in the treated water (SI, Fig. S12).

Double bond equivalent minus the oxygen content per carbon ((DBE-O)/C) and the nominal oxidation state of carbon (NOSC), are commonly used to reflect the unsaturation and redox state of organic molecules, respectively.(He et al., 2024; Seifert et al., 2016) Our grouping analysis indicated that composite coagulants enhanced the removal of oxidized and low-unsaturation reduced organic matter. For compounds with CHO and CHNO molecular formulas, a high unsaturation and a high oxidation state suggest a structure with a larger proportion of heterocyclic carbon atoms and oxygen-containing functional groups, making these compounds more susceptible to removal. In contrast, for CHOS and CHNOS compounds, the presence of sulfur-containing functional groups, which contribute strong electronegativity, enables reduced organic matter to effectively bind to the composite coagulants (SI, Fig. S13). Fig. 3e-f illustrates that the proportion of oxidized substances with high aromaticity (AI_{mod}) can be further removed by composite coagulants (Zhou et al., 2024). This is because more complex carbon chain structures in these substances can form multiple binding sites with Me ions simultaneously. The Kendrick Mass Defect (KMD) analysis revealed that, among molecules with similar structures, those with a higher number of carboxyl groups (-COOH) were more readily removed by the composite coagulant due to their stronger negative electronegativity after ionization (SI, Fig. S14) (Zhu et al., 2023). Furthermore, among homologous compounds with similar molecular weights, those with fewer -CH_2 groups are

more easily removed, suggesting that the weak ionization effect brought by -CH_2 outweighs the increased molecular weight's attraction effect. This indicates that differences in functional groups are the primary factor determining the efficiency of further removal by the composite coagulant (Yuan et al., 2017).

Characterization results of flocs in the solid phase corroborate the above findings. The XPS-C spectrum indicates that, compared to using Fe^{3+} coagulant alone, Ca^{2+} provided the least enhancement, Fe-Ti primarily enhanced the removal of phenolic carbon, while Fe-Zr and Fe-Al composite coagulants significantly increased the binding of both phenolic and carbonyl carbon (Fig. 3h and Table S2) (Yang et al., 2023b). FTIR spectra between 1800 cm^{-1} and 1200 cm^{-1} reflect adsorbed organics on flocs (Li et al., 2020). With an increased dosage of Me, Fe-Al and Fe-Zr composite coagulants enhanced the removal of aromatic (C═C stretching at 1650 cm^{-1}), carboxyl (stretching at 1600 cm^{-1} and 1450 cm^{-1}), aliphatic (1400 cm^{-1}), and unsaturated carbon (C=O of amides or C=N of imines around 1550 cm^{-1}) (Kim and Grassian, 2021; Ma et al., 2024). However, increasing the Ti^{4+} dosage only improved the removal of aromatic substances. Similar results were obtained in HA water, demonstrating the broad applicability of these findings (SI, Fig. S16).

Figure 3

3.4 Changes in phosphate binding mechanisms caused by Fe^{3+}-Me composite coagulants

Previous studies have demonstrated that, during the coagulation process, phosphate can be adsorbed on the flocs surface or embedded into the amorphous structure by co-precipitation, forming multiple configurations between PO_4 tetrahedrons and FeO_6 dimers (Rose et al., 1996). Here, three typical angular linkages between PO_4 tetrahedrons and FeO_6 dimers with significant differences were selected for DFT calculations: the outer-sphere coordination via physical adsorption, binuclear corner-sharing, and mononuclear corner-sharing complex (Rahnemaie et al., 2007; Weng et al., 2020). Fig. 4a presents visualized ESP analysis results. Among these,

the binuclear corner-sharing complex exhibits the lowest positive ESP value (+57.52 kJ/mol, Table S5), while the positive ESP values for the outer-sphere and mononuclear corner-sharing structures were 66.44 kJ/mol and 64.33 kJ/mol, respectively. This indicates that the binuclear corner-sharing complex is more likely to form on the surface of net positively charged flocs. The bond energy between phosphate and FeO_6 clusters reflects the thermodynamic stability of these structures.(Lian et al., 2024; Zhao et al., 2006) The calculations revealed that the P-OFe bond energy in the mononuclear coordination structure was 646.53 kJ/mol, whereas the energy required to break the two P-OFe bonds in the binuclear structure was 1125.91 kJ/mol, indicating the higher thermodynamic stability of binuclear coordination (Table S6). Additionally, differences in the energy band gaps of these similar configurations reflect their inner electronic transition capabilities.(Whangbo et al., 2015) The band gap of the outer-sphere, mononuclear corner-sharing, and binuclear corner-sharing complex were 1.36 eV, 1.23 eV, and 1.99 eV, respectively, suggesting that electron transitions in the binuclear corner-sharing structure are more difficult, and clusters have a more stable existence in this mode (Fig. 4b and SI, Fig. S17).

By analyzing these three optimized models, we discerned the FTIR signals that each configuration may generate. The FTIR spectra of flocs formed by various coagulants were deconvoluted to determine the proportion of phosphate complexes with different configurations on flocs (SI, Fig. S20). 2D-COS elucidates variations in signals at distinct positions as a function of the independent variable (Me dosage), allowing elucidation of the changes in binding modes between flocs formed by different composite coagulants and phosphate as the Me dosage varies (Fig. 4c and Table S7) (Liu et al., 2020). The synchronous results indicate that the primary response peaks were concentrated at 1127 cm^{-1}, 1061 cm^{-1}, 1010 cm^{-1}, and 875 cm^{-1}, corresponding to the vibrations of P=O, symmetric stretching vs(P-OFe), asymmetric stretching vas(P-OFe), and protonated P-OH vibrations, respectively (Li et al., 2021). For flocs formed by Fe-Al, Fe-Ti, and Fe-Zr, the peak at 1010 cm^{-1} exhibited a negative correlation with peaks at 1127 cm^{-1} and 1061 cm^{-1}, which indicated that as the dosage of Me increased, a greater proportion of phosphates was incorporated into flocs via binuclear

corner-sharing, while the proportion of mononuclear corner-sharing phosphates diminished. Asynchronous results revealed that bidentate vibration precedes the monodentate vibration, indicating that higher Me dosages in composite coagulants initially promoted more phosphate binding to the floc in the binuclear corner-sharing complex. Subsequently, a transition from mononuclear to binuclear coordination occurred on the floc surface. Flocs formed in HA water adhered to the same pattern, underscoring the generality of these phosphate configuration changes (SI, Fig. S18).

Furthermore, the protonated phosphate signal on flocs formed by Fe-Al and Fe-Zr composite coagulants showed a positive correlation with Me dosage, suggesting that the proportion of phosphate in the outer sphere complex increases as the quantity of Me escalates. In contrast, Fe-Ti demonstrated an inverse trend: the increase in Ti^{4+} proportion led to a greater concentration of deprotonated phosphate, potentially due to the more negatively charged surface of flocs formed by Fe-Ti (Krumina et al., 2016). Compared to adding Fe coagulant alone, Fe-Al and Fe-Zr increased the proportion of outer sphere-complexed and protonated phosphate. This shift is reflected in the XPS-P_{1p} peaks, which migrated towards higher energy levels (Fang et al., 2022). Conversely, flocs formed by Fe-Ti promoted the deprotonation of surface phosphate, which is consistent with the FTIR findings (Fig. 4f).

The phosphate removal curves of different coagulants were fitted using second-order reaction kinetics (SI, Fig. S19 and Table S8) (Plazinski et al., 2009), indicating that chemical adsorption is the rate-controlling step in coagulation and its rate constant (k) is associated with the type of chemical bond (Wang and Guo, 2020). The calculated reaction rates for phosphate removal are presented in Fig. 4e. The findings demonstrate that increasing the dosage of Al^{3+} and Zr^{4+} significantly enhanced the coagulation reaction rate, leading to more efficient phosphate removal. In contrast, the dosage of Ca^{2+} and Ti^{4+} primarily augments overall phosphate adsorption capacity but does not effectively accelerate the reaction rate. A strong correlation between changes in kinetics and the variations in the contribution of different binding modes (SI, Fig. S20c) shows that the increase in Al^{3+} and Zr^{4+} concentration significantly changes the chemical bonding mode between phosphate and flocs, thereby

enhancing the removal rate of phosphate, which is consistent with the FTIR peak separation results.

The element distribution correlation in EDS results was used to reflect the binding affinity of metal elements with phosphate (Fig. 4g and SI, Fig. S21-S26). The analysis revealed that compared to adding Fe coagulant alone, the Fe element in flocs formed by composite coagulants exhibited a stronger distribution correlation with P. This suggests a tighter binding potential between Fe and phosphate in the co-precipitation process when composite coagulants are employed. Additionally, the correlation between the distribution of Ti and Ca with phosphorus was significantly lower than that of Al and Zr, indicating that Ti and Ca are more prone to heterogeneous nucleation and exhibit a reduced binding potential with phosphate.(Jamoteau et al., 2023) Flocs produced by composite coagulants display less pronounced diffraction patterns in the TEM lens, indicating a more disordered structure (SI, Fig. S27) (Rodenburg, 1999). This distinct amorphous structure is difficult to characterize using conventional methods, necessitating the use of more advanced techniques.(Tamrat et al., 2019)

Figure 4

3.5 Atomic-level changes in cluster structure are the key to causing different coagulation behavior

Fe K-edge EXAFS data of flocs formed by composite coagulants that showed significant improvement (Fe-Al, Fe-Ti, and Fe-Zr) were collected and compared with flocs formed by the Fe coagulant alone to illustrate their improvement in the nanostructure. The Morlet wavelet transform (WT) results (Fig. 5a-b) show the Fe-Fe and corner-sharing Fe-P coordination environment around the second shell of the central Fe atom.

The XANES peak of flocs lies between those of amorphous iron phosphate and crystalline minerals (SI, Fig. S28). A first-order derivative analysis of the absorption signal at 7110 eV-7150 eV, linearly fitted using standard mineral data, revealed that the nanostructure of the flocs

consists of iron oxyhydroxides (such as ferrihydrite) and amorphous iron phosphate (Fig. 5 and Table S9). This suggests that phosphate is not merely adsorbed onto formed iron oxyhydroxide nanoparticles, but rather, it binds around Fe atoms in the early hydrolysis stages, forming a cluster structure that is preserved in co-precipitation. Amorphous iron phosphate compounds in flocs formed by composite coagulants were significantly more abundant than those formed by the Fe coagulant without Me (Daugherty et al., 2017). Conversely, the proportion of ferrihydrite was markedly lower, indicating that the addition of auxiliary Me during coagulation promoted a transformation from amorphous ferrihydrite to an amorphous iron phosphate structure. Furthermore, the ferrihydrite content in flocs formed by Fe-Al, Fe-Ti, and Fe-Zr coagulants was found to be 40%, 31%, and 27%, respectively, indicating that higher atomic numbers of auxiliary Me lead to greater disruption of the ferrihydrite structure within the flocs.

To ensure consistency, shell fitting data were constrained to the same reference path and identical fitting criteria, attributing variations to coordination number and bond length. (Chen et al., 2016) In all flocs, the first coordination shell of Fe atoms, occupied by oxygen atoms with a coordination number of 4 to 6, suggests incomplete hydrolysis of some Fe ions, resulting in a mix of tetrahedral FeO_4 and octahedral FeO_6 configurations.(Hiemstra and Van Riemsdijk, 2009) In the second shell, Fe-Fe bonds with a bond length of approximately 3.04 Å corresponded to Fe atoms sharing two oxygen atoms in edge-coordinated octahedra, indicating the formation of shared-atom dimers or trimers within the flocs. Meanwhile, Fe-Fe bonds with a bond length of around 3.40 Å in the third shell indicated corner-coordinated octahedra, where two FeO_6 shared a single oxygen atom, pointing to the formation of corner-shared trimers within flocs.(Nenonen et al., 2023) Fitting the results revealed that, compared to using Fe coagulant only, the coordination number of Fe-Fe bonds in flocs formed by composite coagulants was significantly reduced. This reduction was more pronounced with an increase in the atomic number of the auxiliary Me. This reduction occurred because the auxiliary Me ions further disrupted the corner- and edge-coordinated FeO_6, which had already been altered by phosphate during the co-hydrolysis process, leading to additional changes in the cluster and

chain structures formed between FeO_6. As a result, the amorphous clusters within the floc structure become more dispersed (Senn et al., 2015).

Additionally, the average bond length of the Fe-P bond exhibited a significant reduction with the presence of Me, decreasing from 3.36 Å for flocs formed without Me to approximately 3.26 Å, which indicates that the corner-sharing mode between PO_4 and FeO_6 had been affected. DFT calculations suggest that the distance between P and Fe atoms in the binuclear corner-sharing structure is notably shorter than that in the mononuclear corner-sharing structure (Lian et al., 2024). This suggests that, compared to the use of Fe^{3+} coagulants alone, phosphates bound to Fe atoms in the flocs formed by the composite coagulant were more likely to form a binuclear corner-sharing complex with a FeO_6 cluster. This is likely due to the increased dispersion of FeO_6 polymers caused by the incorporation of other Me, which exposes more active sites for the binuclear corner-sharing complex with PO_4. Furthermore, in the presence of a more dispersed polymer structure, PO_4 tetrahedra — with their smaller geometric volume — can more readily integrate within it, enhancing the likelihood of the formation of a binuclear corner-sharing complex. The structural changes in the flocs, driven by the doping of auxiliary metals, thus facilitate a more effective interaction between P and Fe atoms, promoting the formation of a more stable, denser basic unit.

The amorphous structural differences of flocs observed at the atomic scale provide insights into the enhanced performance of composite coagulants. Our findings indicate that Me, co-hydrolyzed with Fe^{3+} ions, disrupts the formation of theoretical products and leads to a shift in the floc structure. Initially dominated by amorphous ferrihydrite, these flocs evolve into an even more amorphous form due to the involvement of metal ions. At the macroscopic scale, the integration of Me drives a transformation from iron hydroxide oxides to iron-phosphorus co-precipitates. Microscopically, the inclusion of Me within FeO_6 octahedrals results in a more dispersed cluster configuration and alters the chain architecture. This means that more active sites are exposed and able to link with phosphate tetrahedrons, which improves the utilization efficiency of Fe atoms and forms a more stable complexion with P atoms.

Figure 5

Table 2. Statistical parameters of Fe K-edge EXAFS shell fit for flocs

Sample	*Atom path*	*Reff(Å)*	*CN(±)*	*R(Å) (±)*	*σ^2(Å^2) (±)*	*ΔE_0(eV)*	*R-factor*
Fe-only	Fe-O_1	1.92	1.9(3)	1.94(1)	0.001(3)	2.88 (±0.71)	0.0085
	Fe-O_2	2.04	2.4(4)	2.10(1)	0.001		
	Fe-Fe_{edge-}	3.02	2.6(5)	3.04(1)	0.010		
	Fe-P	3.28	2.4(6)	3.36(3)	0.010		
	Fe-$Fe_{corner-}$	3.40	4.3(6)	3.42(1)	0.012		
Fe-Al^{3+}	Fe-O_1	1.92	2.2(5)	1.95(2)	0.001(3)	2.72 (±0.40)	0.0197
	Fe-O_2	2.04	2.6(5)	2.11(2)	0.001		
	Fe-Fe_{edge-}	3.02	2.2(8)	3.07(3)	0.010		
	Fe-P	3.28	2.2(8)	3.26(5)	0.010		
	Fe-$Fe_{corner-}$	3.40	3.9(9)	3.38(2)	0.012		
Fe-Ti^{4+}	Fe-O_1	1.92	2.0(3)	1.95(2)	0.001(3)	2.26 (±0.29)	0.0085
	Fe-O_2	2.04	2.2(3)	2.11(2)	0.001		
	Fe-Fe_{edge-}	3.02	1.6(5)	3.05(2)	0.010		
	Fe-P	3.28	2.0(5)	3.27(3)	0.010		
	Fe-$Fe_{corner-}$	3.40	3.1(5)	3.39(1)	0.012		
Fe-Zr^{4+}	Fe-O_1	1.92	1.7(3)	1.93(2)	0.001(3)	1.46 (±0.28)	0.007
	Fe-O_2	2.04	2.1(3)	2.08(2)	0.001		
	Fe-Fe_{edge-}	3.02	1.3(4)	3.01(2)	0.010		
	Fe-P	3.28	2.2(5)	3.28(3)	0.010		
	Fe-$Fe_{corner-}$	3.40	2.5(5)	3.41(5)	0.012		

The passive amplitude reduction factor, S_0^2, was fixed at 0.8 for Fe. The number of variables is 7 out of a total of 15.34 independent data points.

Data ranges: 2.5 Å ≤ k ≤ 11.5 Å, 1.0 Å ≤R≤3.75 Å.

CN: Coordination number.

R: half path length.

Reff: half path length of reference.

The Debye−Waller parameters, σ^2, were fixed at 0.01 Å^2 (Fe-Fe_{edge-}), 0.01 Å^2 (Fe−P), and 0.012 Å^2 (Fe-$Fe_{corner-}$)

Shell fitting was performed layer-by-layer, and σ^2 of each shell was fixed to the same.

4. Conclusions

Coagulation, a cost-effective and time-tested water treatment process, is widely employed to improve water quality. The increasing complexity of pollutants necessitates the development of more advanced and effective coagulants. This study has evaluated composite coagulants incorporating additional metals, investigating their effects and mechanisms to address the limitations of conventional Fe coagulants and guide future coagulant development. The results reveal that Al^{3+}, Ti^{4+}, and Zr^{4+} ions significantly enhance phosphorus removal and floc size across different water types. Notably, Al^{3+} and Zr^{4+} further optimized the removal of hydrophobic macromolecules and medium-sized NOM with complex structures, including polycarboxyl, aromatic, and secondary carbon components.

Our research has demonstrated that the co-hydrolysis of multiple Me during coagulation is not a simple, non-interfering process, and atomic-level evidence is provided in this study. The presence of different Me can alter the amorphous structure of FeOOH at the nanoscale, thereby influencing the macroscopic coagulation behavior. The hydrolysis products of Me in composite coagulants bond within flocs, which significantly alters the nanostructure of conventional flocs by dispersing links between FeO_6 octahedra dimer, thus promoting a tighter and more stable binding configuration between FeO_6 octahedra and PO_4 tetrahedrons.

We emphasize the importance of structural changes within amorphous flocs in enhancing coagulation efficiency. This study demonstrates that amorphous structures in environmental processes, although complex, are not incapable of analysis through careful investigation. Often overlooked, the transformations of amorphous structures play a critical role in environmental engineering, particularly in coagulation. Insights into the interactions between multiple Me during floc formation enhance our understanding of their key roles in environmental engineering and co-precipitation processes in geochemical cycles.

Acknowledgments

This study was financially supported by the International Partnership Program of the Chinese Academy of Sciences (Grant No.309GJHZ2023003MI and No.032GJHZ2023063MI) and National Natural Science Foundation of China (Grant No. 52370184).

X-ray absorption spectroscopy analyses were performed at the BL14W1 beamlines at the Shanghai Synchrotron Radiation Facility (SSRF) (China).

Notes

The authors declare no competing interests.

References

2002 Environmental quality standards for surface water, https://www.mee.gov.cn/ywgz/fgbz/bz/bzwb/shjbh/shjzlbz/200206/t20020601_66497.shtml.

Anderson, D.M., Glibert, P.M. and Burkholder, J.M. 2002. Harmful algal blooms and eutrophication: Nutrient sources, composition, and consequences. Estuaries 25(4b), 704-726.

Cao, X.D., Ma, L.Q., Chen, M., Singh, S.P. and Harris, W.G. 2002. Impacts of phosphate amendments on lead biogeochemistry at a contaminated site. Environ Sci Technol 36(24), 5296-5304.

Chen, C.M., Dynes, J.J., Wang, J. and Sparks, D.L. 2014. Properties of Fe-Organic Matter Associations via Coprecipitation versus Adsorption. Environ Sci Technol 48(23), 13751-13759.

Chen, K.Y., Chen, T.Y., Chan, Y.T., Cheng, C.Y., Tzou, Y.M., Liu, Y.T. and Teah, H.Y. 2016. Stabilization of Natural Organic Matter by Short-Range-Order Iron Hydroxides. Environ Sci Technol 50(23), 12612-12620.

Chen, W., Qian, C., Zhou, K.G. and Yu, H.Q. 2018. Molecular Spectroscopic Characterization of Membrane Fouling: A Critical Review. Chem-Us 4(7), 1492-1509.

Collins, R.N., Rosso, K.M., Rose, A.L., Glover, C.J. and Waite, T.D. 2016. An XAS study of ferric iron hydrolysis and precipitation in the presence of perchlorate, nitrate, chloride and sulfate. Geochim Cosmochim Ac 177, 150-169.

Correll, D.L. 1998. The role of phosphorus in the eutrophication of receiving waters: A review. J Environ Qual 27(2), 261-266.

Das, B. 2018. Theoretical Study of Small Iron-Oxyhydroxide Clusters and Formation of Ferrihydrite. J Phys Chem A 122(2), 652-661.

Daugherty, E.E., Gilbert, B., Nico, P.S. and Borch, T. 2017. Complexation and Redox Buffering of Iron(II) by Dissolved Organic Matter. Environ Sci Technol 51(19), 11096-11104.

Dayarathne, H.N.P., Angove, M.J., Aryal, R., Abuel-Naga, H. and Mainali, B. 2021. Removal of natural organic matter from source water: Review on coagulants, dual coagulation, alternative coagulants, and mechanisms. J Water Process Eng 40.

Ding, Q., Ishikawa, D., Yamamura, H. and Watanabe, Y. 2024. Causes of negatively charged meso-colloids formed in the coagulation process: Implication of the origin of foulants in the coagulation-membrane filtration process. Water Res 266.

Douterelo, I., Dutilh, B.E., Calero, C., Rosales, E., Martin, K. and Husband, S. 2020. Impact of phosphate dosing on the microbial ecology of drinking water distribution systems: Fieldwork studies in chlorinated networks. Water Res 187.

Duan, J.M. and Gregory, J. 2003. Coagulation by hydrolysing metal salts. Adv Colloid Interfac 100, 475-502.

Fang, D.X., Huang, L.P., Fan, J.P., Xiao, H., Wu, G.X., Wang, Y.J., Zeng, Z.X., Shen, F., Deng, S.H. and Ji, F.Y. 2022. New insights into the arrangement pattern of

layered double hydroxide nanosheets and their ion-exchange behavior with phosphate. Chem Eng J 441.

Frenkel, A.I., Hills, C.W. and Nuzzo, R.G. 2001. A view from the inside: Complexity in the atomic scale ordering of supported metal nanoparticles. J Phys Chem B 105(51), 12689-12703.

Gan, Y., Wang, X., Zhang, L., Wu, B., Zhang, G. and Zhang, S. 2019. Coagulation removal of fluoride by zirconium tetrachloride: Performance evaluation and mechanism analysis. Chemosphere 218, 860-868.

Gentile, L., Wang, T., Tunlid, A., Olsson, U. and Persson, P. 2018. Ferrihydrite Nanoparticle Aggregation Induced by Dissolved Organic Matter. J Phys Chem A 122(38), 7730-7738.

Guo, X.L., Yang, K.L., Fu, H., Xia, Q.F., Wang, T. and Yang, S.H. 2017. Ice processes modeling during reverse water transfer of open canals: A case study. J Hydro-Environ Res 17, 56-67.

He, Y.T., Jarvis, P., Huang, X. and Shi, B.Y. 2024. Unraveling the characteristics of dissolved organic matter removed by aluminum species based on FT-ICR MS analysis. Water Res 255.

Henneberry, Y.K., Kraus, T.E.C., Nico, P.S. and Horwath, W.R. 2012. Structural stability of coprecipitated natural organic matter and ferric iron under reducing conditions. Org Geochem 48, 81-89.

Hiemstra, T. 2018. Ferrihydrite interaction with silicate and competing oxyanions: Geometry and Hydrogen bonding of surface species. Geochim Cosmochim Ac 238, 453-476.

Hiemstra, T. and Van Riemsdijk, W.H. 2009. A surface structural model for ferrihydrite I: Sites related to primary charge, molar mass, and mass density. Geochim Cosmochim Ac 73(15), 4423-4436.

Hotze, E.M., Phenrat, T. and Lowry, G.V. 2010. Nanoparticle Aggregation: Challenges to Understanding Transport and Reactivity in the Environment. J Environ Qual 39(6), 1909-1924.

Jamoteau, F., Cam, N., Levard, C., Doelsch, E., Gassier, G., Duvivier, A., Boulineau, A., Saint-Antonin, F. and Basile-Doelsch, I. 2023. Structure and Chemical Composition of Soil C-Rich Al-Si-Fe Coprecipitates at Nanometer Scale. Environ Sci Technol 57(49), 20615-20626.

Jarvis, P., Sharp, E., Pidou, M., Molinder, R., Parsons, S.A. and Jefferson, B. 2012. Comparison of coagulation performance and floc properties using a novel zirconium coagulant against traditional ferric and alum coagulants. Water Res 46(13), 4179-4187.

Kim, D. and Grassian, V.H. 2021. Attenuated Total Reflection-Fourier Transform Infrared and Atomic Force Microscopy-Infrared Spectroscopic Investigation of Suwannee River Fulvic Acid and Its Interactions with α-FeOOH. Acs Earth Space Chem 6(1), 81-89.

Kraal, P., Van Genuchten, C.M. and Behrends, T. 2022. Phosphate coprecipitation affects reactivity of iron (oxyhydr)oxides towards dissolved iron and sulfide. Geochim

Cosmochim Ac 321, 311-328.

Krumina, L., Kenney, J.P.L., Loring, J.S. and Persson, P. 2016. Desorption mechanisms of phosphate from ferrihydrite and goethite surfaces. Chem Geol 427, 54-64.

Kubicki, J.D., Paul, K.W., Kabalan, L., Zhu, Q., Mrozik, M.K., Aryanpour, M., Pierre-Louis, A.M. and Strongin, D.R. 2012. ATR-FTIR and Density Functional Theory Study of the Structures, Energetics, and Vibrational Spectra of Phosphate Adsorbed onto Goethite. Langmuir 28(41), 14573-14587.

LaGrow, A.P., Besenhard, M.O., Hodzic, A., Sergides, A., Bogart, L.K., Gavriilidis, A. and Thanh, N.T.K. 2019. Unravelling the growth mechanism of the co-precipitation of iron oxide nanoparticles with the aid of synchrotron X-Ray diffraction in sotution. Nanoscale 11(14), 6620-6628.

Lartiges, B., El Samrani, A.G., Montargès-Pelletier, E., Bihannic, I., Briois, V. and Michot, L. 2019. Aggregating ability of ferric chloride in the presence of phosphate ligand. Water Res 164.

Li, J.F., Li, J.G., Liu, X.Y., Du, Z.P. and Cheng, F.Q. 2018. Effect of silicon content on preparation and coagulation performance of poly-silicic-metal coagulants derived from coal gangue for coking wastewater treatment. Sep Purif Technol 202, 149-156.

Li, S.Q., Guo, Y., Zhang, X., Feng, L., Yong, X.L., Xu, J., Liu, Y.C. and Huang, X. 2023a. Advanced nitrogen and phosphorus removal by the symbiosis of PAOs, DPAOs and DGAOs in a pilot-scale A2O/A+MBR process with a low C/N ratio of influent. Water Res 229.

Li, X.C., Yan, L., Zhong, W., Kersten, M. and Jing, C.A.Y. 2021. Competitive arsenate and phosphate adsorption on α-FeOOH, LaOOH, and nano-TiO
: Two-dimensional correlation spectroscopy study. J Hazard Mater 414.

Li, Y.Y., Wang, Y.D., Jin, J., Tian, Z.Q., Yang, W.B., Graham, N.J.D. and Yang, Z. 2023b. Enhanced removal of trace pesticides and alleviation of membrane fouling using hydrophobic-modified inorganic-organic hybrid flocculants in the flocculation-sedimentation-ultrafiltration process for surface water treatment. Water Res 229.

Li, Z.X., Shakiba, S., Deng, N., Chen, J.W., Louie, S.M. and Hu, Y.D. 2020. Natural Organic Matter (NOM) Imparts Molecular-Weight-Dependent Steric Stabilization or Electrostatic Destabilization to Ferrihydrite Nanoparticles. Environ Sci Technol 54(11), 6761-6770.

Lian, W.L., Yu, G.H., Ma, J., Xiong, J., Niu, C.Y., Zhang, R., Xie, H.J. and Weng, L.P. 2024. Quantitative Insights into Phosphate-Enhanced Lead Immobilization on Goethite. Environ Sci Technol 58(26), 11748-11759.

Liu, B., Gao, Y., Pan, J., Feng, Q., Yue, Q., Guo, K. and Gao, B. 2022. Coagulation behavior of polyaluminum-titanium chloride composite coagulant with humic acid: A mechanism analysis. Water Res 220, 118633.

Liu, B.B., Guo, K.Y., Yue, Q.Y., Gao, Y. and Gao, B.Y. 2024a. Uncovering the performance and intrinsic mechanism of different hydrolyzed AlTi species in

671 polystyrene nanoplastics coagulation. Water Res 266.
672 Liu, J.W., Fu, T., Sun, G.D., Shen, X.R., Liu, S., He, Y., Xu, Y. and Zhao, H.Z.
673 2023. A versatile organic silicate aluminum hybrid coagulant for broad-spectrum
674 removal of heavy metal ions. Chem Eng J 472.
675 Liu, M., Liu, X., Graham, N.J.D. and Yu, W. 2024b. Uncovering the neglected
676 role of anions in trivalent cation-based coagulation processes. Water Res 254, 121352.
677 Liu, M.J., Graham, N., Gregory, J., Elimelech, M. and Yu, W.Z. 2024c. Towards
678 a molecular-scale theory for the removal of natural organic matter by coagulation with
679 trivalent metals. Nat Water 2(3), 285-294.
680 Liu, X.Y., Chen, W. and Yu, H.Q. 2020. Probing protein-induced membrane
681 fouling with attenuated total reflectance fourier transform infrared spectroscopy and
682 multivariate curve resolution-alternating least squares. Water Res 183.
683 Lu, T. 2024. A comprehensive electron wavefunction analysis toolbox for
684 chemists, Multiwfn. J Chem Phys 161(8).
685 Ma, W.W., He, J.H., Han, L.F., Ma, C.X., Cai, Y.P., Guo, X.Y. and Yang, Z.F. 2024.
686 Hydrophilic Fraction of Dissolved Organic Matter Largely Facilitated Microplastics
687 Photoaging: Insights from Redox Properties and Reactive Oxygen Species. Environ Sci
688 Technol 58(26), 11625-11636.
689 Matilainen, A., Vepsäläinen, M. and Sillanpää, M. 2010. Natural organic matter
690 removal by coagulation during drinking water treatment: A review. Adv Colloid Interfac
691 159(2), 189-197.
692 Mertens, J., Rose, J., Wehrli, B. and Furrer, G. 2016. Arsenate uptake by Al
693 nanoclusters and other Al-based sorbents during water treatment. Water Res 88, 844-
694 851.
695 Nenonen, V.V., Kaegi, R., Hug, S.J., Gottlicher, J., Mangold, S., Winkel, L.H.E.
696 and Voegelin, A. 2023. Formation and transformation of Fe(III)- and Ca-precipitates
697 in aqueous solutions and effects on phosphate retention over time. Geochim
698 Cosmochim Ac 360, 207-230.
699 Pincus, L.N., Rudel, H.E., Petrovic, P.V., Gupta, S., Westerhoff, P., Muhich, C.L.
700 and Zimmerman, J.B. 2020. Exploring the Mechanisms of Selectivity for
701 Environmentally Significant Oxo-Anion Removal during Water Treatment: A Review
702 of Common Competing Oxo-Anions and Tools for Quantifying Selective Adsorption.
703 Environ Sci Technol 54(16), 9769-9790.
704 Plazinski, W., Rudzinski, W. and Plazinska, A. 2009. Theoretical models of
705 sorption kinetics including a surface reaction mechanism: A review. Adv Colloid
706 Interfac 152(1-2), 2-13.
707 Rahnemaie, R., Hiemstra, T. and van Riemsdijk, W.H. 2007. Geometry, charge
708 distribution, and surface speciation of phosphate on goethite. Langmuir 23(7), 3680-
709 3689.
710 Rehr, J.J. and Albers, R.C. 2000. Theoretical approaches to x-ray absorption fine
711 structure. Rev Mod Phys 72(3), 621-654.
712 Rezania, S., Kadi, A., Kamyab, H., Ghfar, A.A., Nodeh, H.R. and Ibrahim, W.N.W.

2022. Lanthanum doped magnetic polyaniline for removal of phosphate ions from water. Chemosphere 307.

Rodenburg, J.M. 1999. Measurement of higher-order correlation functions in amorphous materials via coherent microdiffraction. Inst Phys Conf Ser (161), 145-148.

Rose, J., Manceau, A., Bottero, J.Y., Masion, A. and Garcia, F. 1996. Nucleation and growth mechanisms of Fe oxyhydroxide in the presence of PO4 ions .1. Fe K-edge EXAFS study. Langmuir 12(26), 6701-6707.

Seifert, A.G., Roth, V.N., Dittmar, T., Gleixner, G., Breuer, L., Houska, T. and Marxsen, J. 2016. Comparing molecular composition of dissolved organic matter in soil and stream water: Influence of land use and chemical characteristics. Sci Total Environ 571, 142-152.

Senn, A.C., Kaegi, R., Hug, S.J., Hering, J.G., Mangold, S. and Voegelin, A. 2015. Composition and structure of Fe(III)-precipitates formed by Fe(II) oxidation in water at near-neutral pH: Interdependent effects of phosphate, silicate and Ca. Geochim Cosmochim Ac 162, 220-246.

Shi, Q.T., Jing, C.Y. and Meng, X.G. 2018. Competing Interactions of As Adsorption and Fe(III) Polymerization during Ferric Coprecipitation Treatment. Environ Sci Technol 52(13), 7343-7350.

Smotraiev, R., Nehrii, A., Koltsova, E., Anohina, A., Sorochkina, K. and Ratnaweera, H. 2022. Comparison of wastewater coagulation efficiency of pre-polymerised zirconium and traditional aluminium coagulants. J Water Process Eng 47.

Son, D., Cho, S., Nam, J., Lee, H. and Kim, M. 2020. X-ray-Based Spectroscopic Techniques for Characterization of Polymer Nanocomposite Materials at a Molecular Level. Polymers-Basel 12(5).

Su, Z.Y., Liu, T., Li, X., Graham, N. and Yu, W.Z. 2021. Beneficial impacts of natural biopolymers during surface water purification by membrane nanofiltration. Water Res 201.

Tamrat, W.Z., Rose, J., Grauby, O., Doelsch, E., Levard, C., Chaurand, P. and Basile-Doelsch, I. 2019. Soil organo-mineral associations formed by co-precipitation of Fe, Si and Al in presence of organic ligands. Geochim Cosmochim Ac 260, 15-28.

Unsworth, E.R., Warnken, K.W., Zhang, H., Davison, W., Black, F., Buffle, J., Cao, J., Cleven, R., Galceran, J., Gunkel, P., Kalis, E., Kistler, D., Van Leeuwen, H.P., Martin, M., Noël, S., Nur, Y., Odzak, N., Puy, J., Van Riemsdijk, W., Sigg, L., Temminghoff, E., Tercier-Waeber, M.L., Toepperwien, S., Town, R.M., Weng, L.P. and Xue, H.B. 2006. Model predictions of metal speciation in freshwaters compared to measurements by in situ techniques. Environ Sci Technol 40(6), 1942-1949.

Wang, J.L. and Guo, X. 2020. Adsorption kinetic models: Physical meanings, applications, and solving methods. J Hazard Mater 390.

Wang, Q.X., Tian, C.H., Shi, B.Y., Wang, D.S. and Feng, C.H. 2023a. Efficiency and mechanism of micro- and nano-plastic removal with polymeric Al-Fe bimetallic coagulants: Role of Fe addition. J Hazard Mater 448.

Wang, X.M., Li, M.H., Song, X.J., Chen, Z.H., Wu, B.D. and Zhang, S.J. 2016.

Preparation and Evaluation of Titanium-Based Xerogel as a Promising Coagulant for Water/Wastewater Treatment. Environ Sci Technol 50(17), 9619-9626.

Wang, X.Y., Shi, C., Hao, X.D., van Loosdrecht, M.C.M. and Wu, Y.Y. 2023b. Synergy of phosphate recovery from sludge-incinerated ash and coagulant production by desalinated brine. Water Res 231.

Wang, Y.L., Li, Y.N., Wang, W.H., Tian, L.P., Jia, R.B., Song, W.C. and Ju, L. 2020. The influence of coagulation mechanism on coagulation effects under different Al-based coagulants conditions. Desalin Water Treat 204, 204-212.

Weng, Y.T., Vekeman, J., Zhang, H.L., Chou, L., Elskens, M. and Tielens, F. 2020. Unravelling phosphate adsorption on hydrous ferric oxide surfaces at the molecular level. Chemosphere 261.

Whangbo, M.H., Gordon, E.E., Xiang, H., Koo, H.J. and Lee, C. 2015. Prediction of Spin Orientations in Terms of HOMO-LUMO Interactions Using Spin-Orbit Coupling as Perturbation. Accounts Chem Res 48(12), 3080-3087.

Xu, L., Zhang, Z., Graham, N.J.D. and Yu, W. 2024a. Exploring the influence of aquatic phosphate on Fe floc dynamics in water treatment. Water Res 262, 122146.

Xu, L., Zhang, Z.X., Graham, N.J.D. and Yu, W.Z. 2024b. Exploring the influence of aquatic phosphate on Fe floc dynamics in water treatment. Water Res 262.

Xue, W.J., Zhang, F.F., Zhang, K.F., Sun, J.Q., Ding, W.D., Zhang, Q.W. and Li, Z.P. 2024. Enhanced separation and antifouling performance of ultrafiltration for surface water based on coagulation pretreatment by zirconium salts. Sep Purif Technol 334.

Yang, B.Q., Graham, N., Liu, P., Liu, M.J., Gregory, J. and Yu, W.Z. 2023a. Atomic-Level Structural Differences between Fe(III) Coprecipitates Generated by the Addition of Fe(III) Coagulants and by the Oxidation of Fe(II) Coagulants Determine Their Coagulation Behavior in Phosphate and DOM Removal. Environ Sci Technol 57(33), 12489-12500.

Yang, B.Q., Rashid, S., Graham, N., Li, G.B. and Yu, W.Z. 2023b. In-depth study of the removal of Mn(II) by Fe(VI) treatment and the profound influence of NOM on floc formation and properties. Water Res 247.

Yoshizawa, K. 2012. An Orbital Rule for Electron Transport in Molecules. Accounts Chem Res 45(9), 1612-1621.

Yuan, Z.W., He, C., Shi, Q., Xu, C.M., Li, Z.S., Wang, C.Z., Zhao, H.Z. and Ni, J.R. 2017. Molecular Insights into the Transformation of Dissolved Organic Matter in Landfill Leachate Concentrate during Biodegradation and Coagulation Processes Using ESI FT-ICR MS. Environ Sci Technol 51(14), 8110-8118.

Zhang, C.F., Zhang, L., Liu, J.J., Li, X.Y., Zhang, Q. and Peng, Y.Z. 2024. Achieving ultra-high nitrogen and phosphorus removal from real municipal wastewater in a novel continuous-flow anaerobic/aerobic/anoxic process via partial nitrification, endogenous denitrification and nitrite-type denitrifying phosphorus removal. Water Res 250.

Zhang, L., Ji, L., Liu, X., Zhu, X., Ning, K. and Wang, Z. 2022. Linkage and

driving mechanisms of antibiotic resistome in surface and ground water: Their responses to land use and seasonal variation. Water Res 215.

Zhao, H.Z., Wang, L., Hanigan, D., Westerhoff, P. and Ni, J.R. 2016. Novel Ion-Exchange Coagulants Remove More Low Molecular Weight Organics than Traditional Coagulants. Environ Sci Technol 50(7), 3897-3904.

Zhao, Y., Schultz, N.E. and Truhlar, D.G. 2006. Design of density functionals by combining the method of constraint satisfaction with parametrization for thermochemistry, thermochemical kinetics, and noncovalent interactions. J Chem Theory Comput 2(2), 364-382.

Zhou, P., Tian, L., Siddique, M.S., Song, S., Graham, N.J.D., Zhu, Y.G. and Yu, W.Z. 2024. Divergent Fate and Roles of Dissolved Organic Matter from Spatially Varied Grassland Soils in China During Long-Term Biogeochemical Processes. Environ Sci Technol 58(2), 1164-1176.

Zhu, S.S., Luo, W.D., Mo, Y.J., Ding, K.B., Zhang, M.Y., Jin, C., Wang, S.Z., Chao, Y.Q., Tang, Y.T. and Qiu, R.L. 2023. New Insights into the Role of Natural Organic Matter in Fe-Cr Coprecipitation: Importance of Molecular Selectivity. Environ Sci Technol 57(37), 13991-14001.

Zhuang, J.Y., Qi, Y.H., Yang, H.Z., Li, H.Y. and Shi, T.H. 2021. Preparation of polyaluminum zirconium silicate coagulant and its performance in water treatment. J Water Process Eng 41.

Click here to access/download;Figure;fig1.pdf

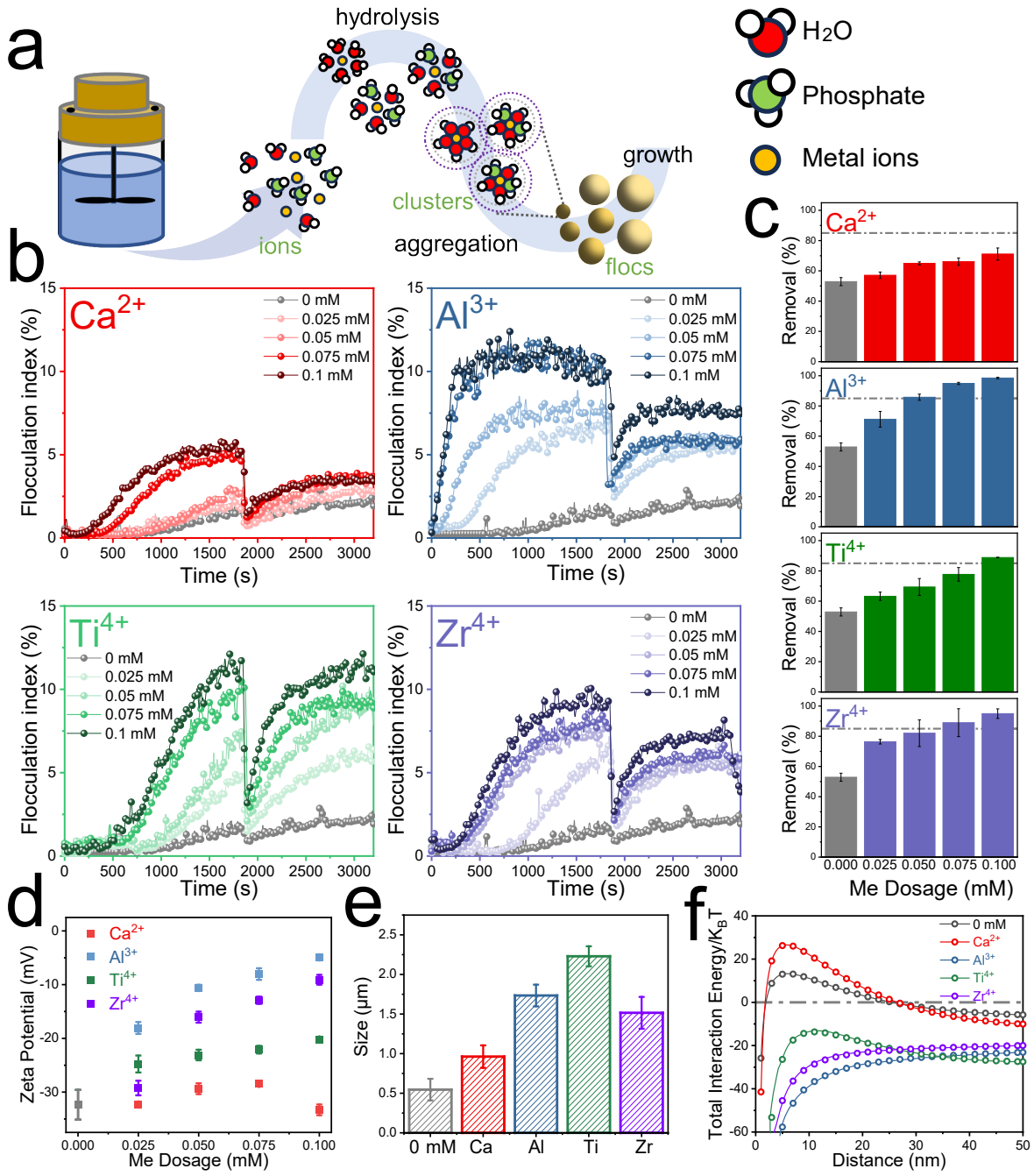


Figure 1. Improvement of different types of Me ions on Fe(III) coagulation when treating phosphate-containing raw water. (a) Schematic diagram of flocs formation in coagulation process when Me ions treat phosphate-containing water. (b) Changes in floc size (FI) over time when using different types of Fe-Me coagulants. The phosphate removal rate (c) and zeta potential (d) after coagulation. Flocs size formed by composite coagulants measured in growth balance (e) when using 0.1 mM Me ions and their interaction forces between particles calculated using the DLVO theory (f).

Click here to access/download;Figure;fig2.pdf

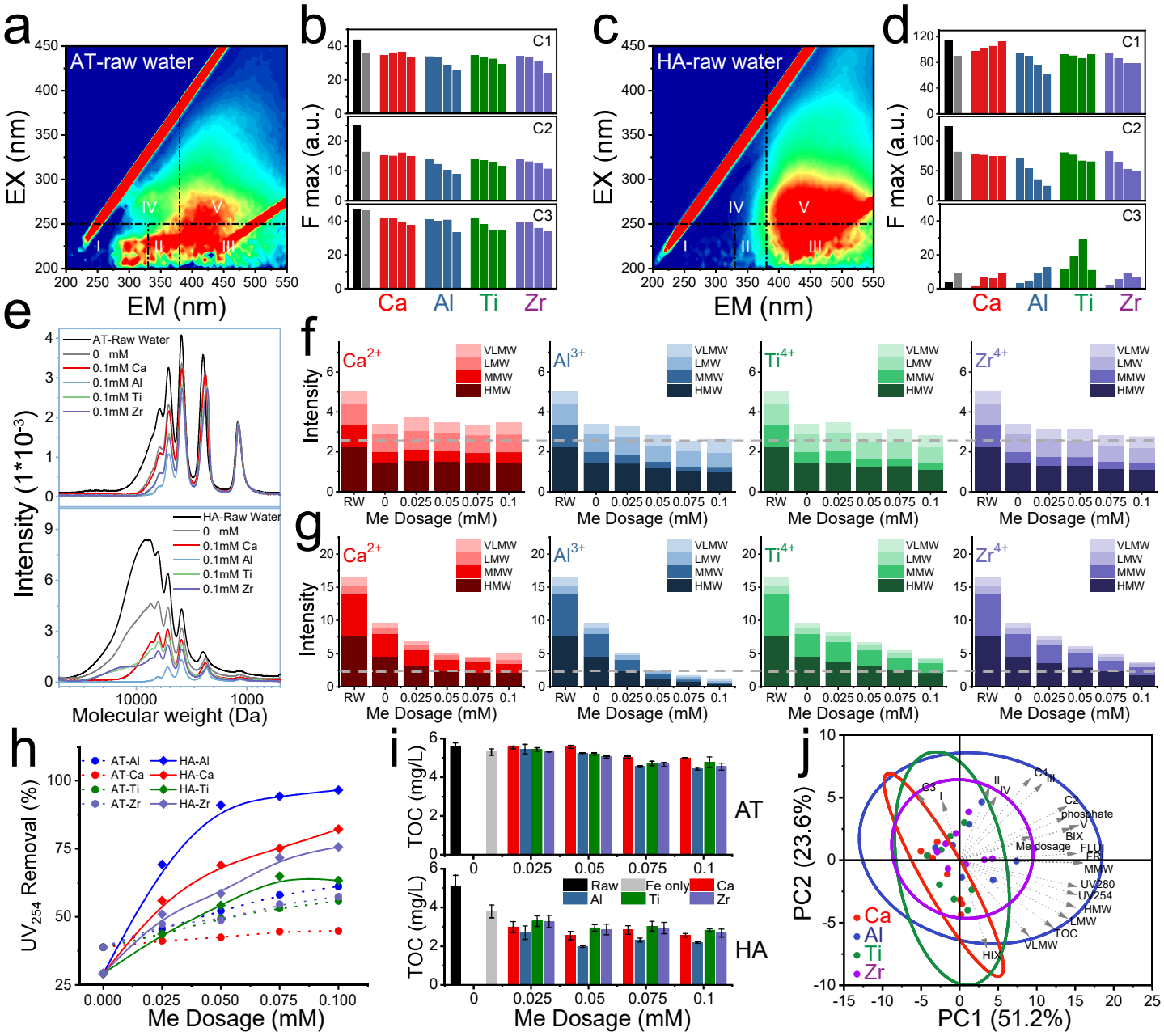


Figure 2. NOM removal from AT and HA water treated with different coagulants. Fluorescence properties of raw AT water (a) and EEM intensity of its components before and after coagulation with different Me concentrations identified by PARAFAC (b). Fluorescence properties of raw HA water (c) and EEM intensity of its components before and after coagulation with different Me concentrations identified by PARAFAC (d) (detailed information on each component can be found in Fig. S4). Changes in molecular weight distribution (e) and relative molecular weight abundance of DOM in AT (f) and HA (g) water before and after coagulation by composite coagulants with different Me concentrations

(VLMW: 0.1k–1.5k Da; LMW:1.5k–4.5k Da; MMW: 4.5k–25k Da; HMW: 25k–100k Da). UV_{254} removal of HA (solid line) and AT (dotted line) water after coagulation (h). TOC of HA and AT water before and after coagulation (i). Differences in DOM indicators of AT and HA water after treatment with different coagulants shown by principal component analysis (PCA) (j) (BIX: biological index; HIX: humification index; FRI: freshness index; FLUI: fluorescence index).

Click here to access/download;Figure;fig3.pdf

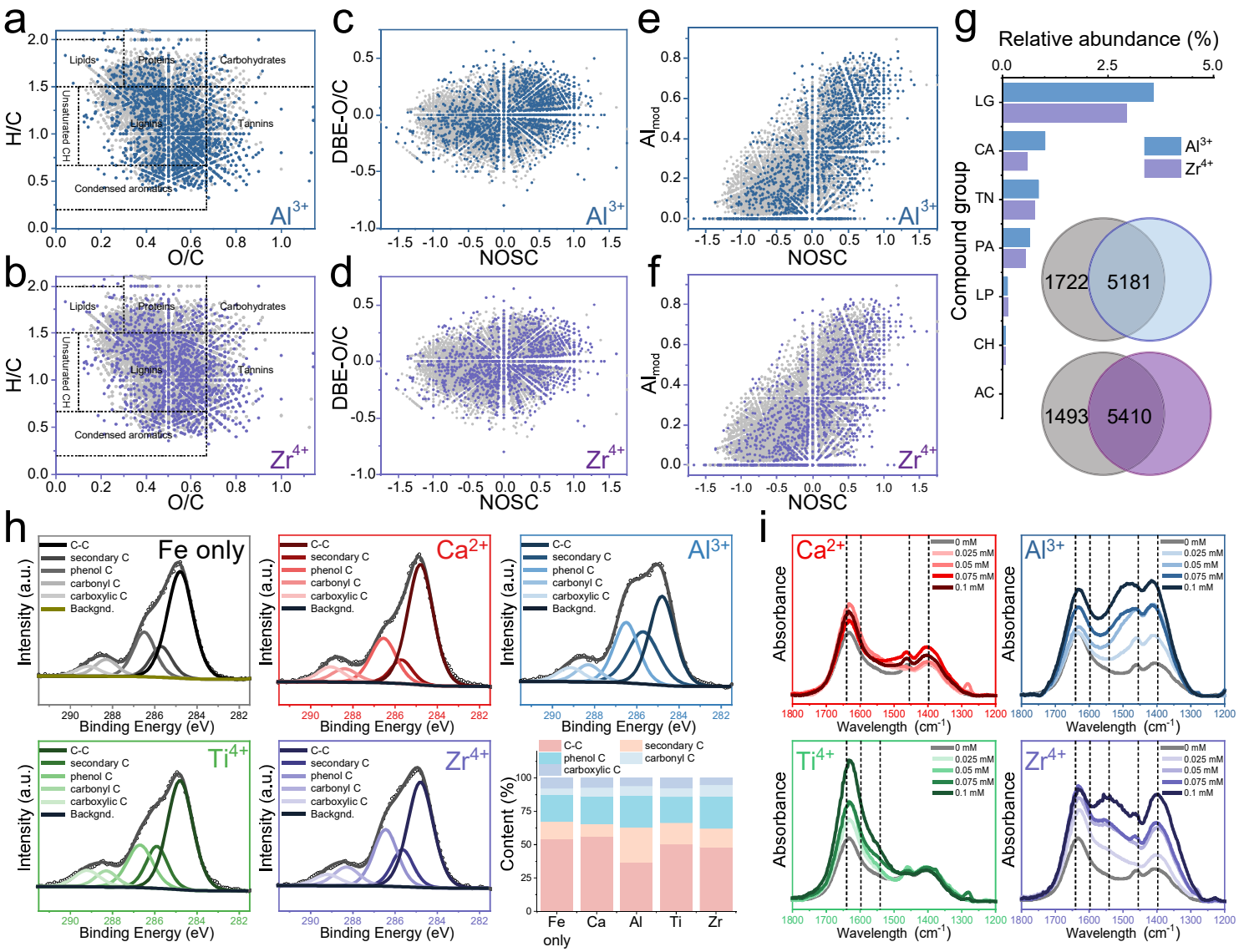


Figure 3. Molecular insights into the enhancement of DOM removal by composite Fe^{3+}-Me coagulants. Van Krevelen diagram (a, b), NOSC vs. (DBE-O)/C diagram (c, d), and NOSC vs. AI_{mod} diagram (e, f) of resistant (grey) and further removed formulas in AT water treated by Fe-Al (blue) and Fe-Ti (violet) composite coagulant compared with Fe(III) coagulant only. The relative abundance of further removed organics by Fe-Al (blue) and Fe-Ti (violet) coagulants compared with the control coagulant and Venn diagram of molecule number in AT water after coagulation with Fe(III) only (grey), Fe-Al (blue), and Fe-Ti (violet) (g). High-resolution C1s XPS spectra of flocs formed by Fe-Me coagulant in AT water with Me addition of 0.1 mM and the content of C in different forms calculated from it (h). The FTIR spectra at 1200-1800 cm^{-1} of flocs formed by Fe-Me coagulant in AT water with different Me concentrations (i).

Click here to access/download;Figure;fig4.pdf

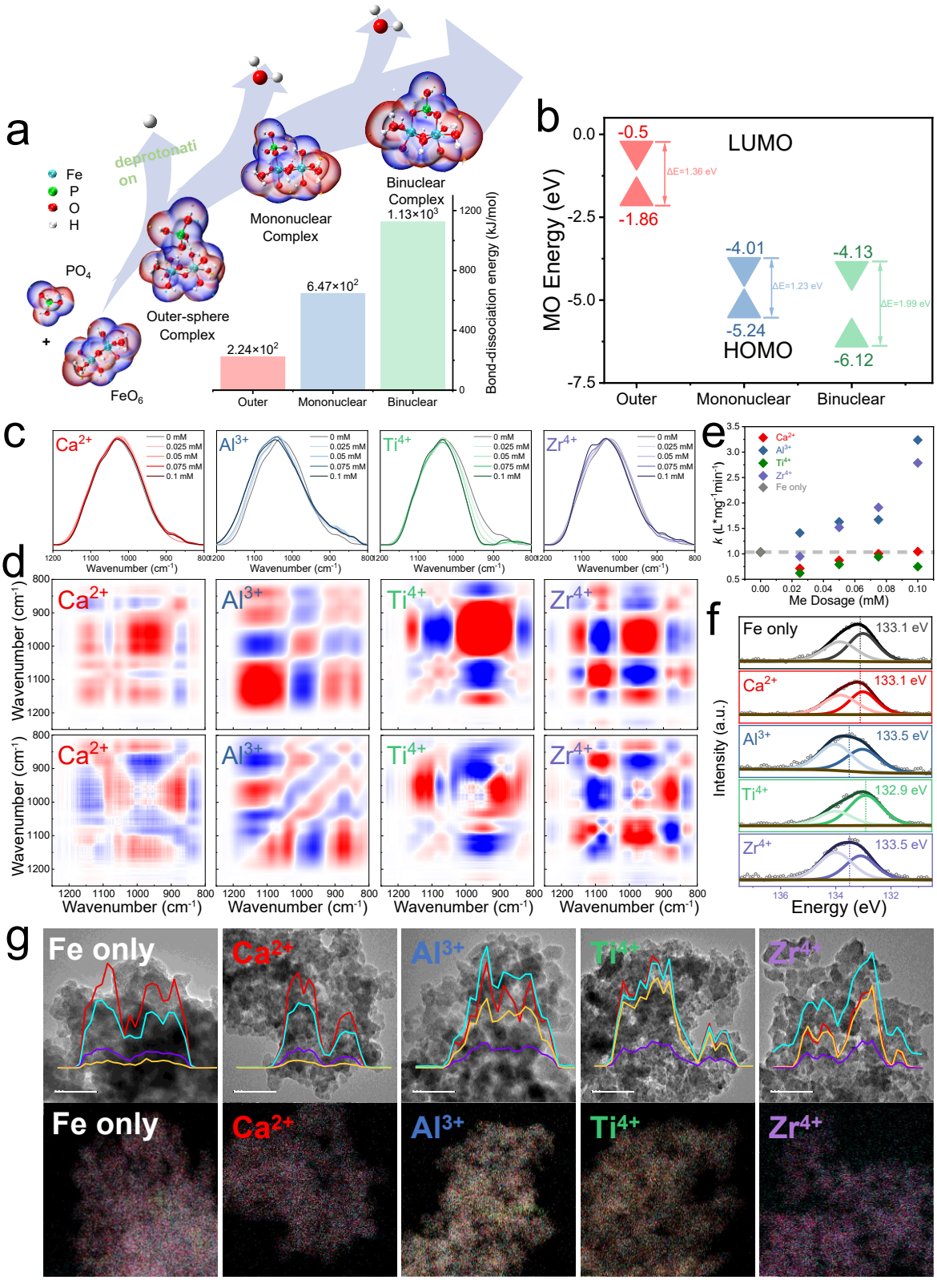


Figure 4. The binding mechanism and behavior of phosphate in flocs is formed by different coagulants in AT water. The structures of clusters formed by Fe and phosphate through three complex states (outer-sphere, mononuclear, and binuclear corner-sharing

complex). Their van-der-Waals surface with electrostatic potential (ESP) optimized by DFT and the bar graph shows the required bonding energy between phosphate and FeO_6 clusters when forming different complexations (a). HOMO-LUMO gap of these clusters (b). Normalized FTIR spectra at 1200-800 cm^{-1} of flocs formed by Fe-Me at different Me concentrations (c), and synchronous and asynchronous 2D-COS maps calculated from it (d) (The variable is the concentration of used Me, red represents positive correlation and blue represents negative correlation, deeper color intensity suggests a stronger positive or negative correlation.). Kinetic constants of phosphate removal by different Fe-Me coagulants (e) (The experimental results were fitted by pseudo-second-order reaction; details are shown in the SI). High-resolution P1p XPS spectra of flocs formed by Fe-Me coagulant in AT water with Me addition of 0.1 mM (f) (The dotted line represents the maximum of the peak). The HRTEM and EDS mapping results of flocs formed by Fe-Me coagulant in AT water with Me addition of 0.1 mM (g) (O: cyan; Fe: red; P: purple; Me: orange; details are shown in the SI).

Click here to access/download;Figure;fig5.pdf

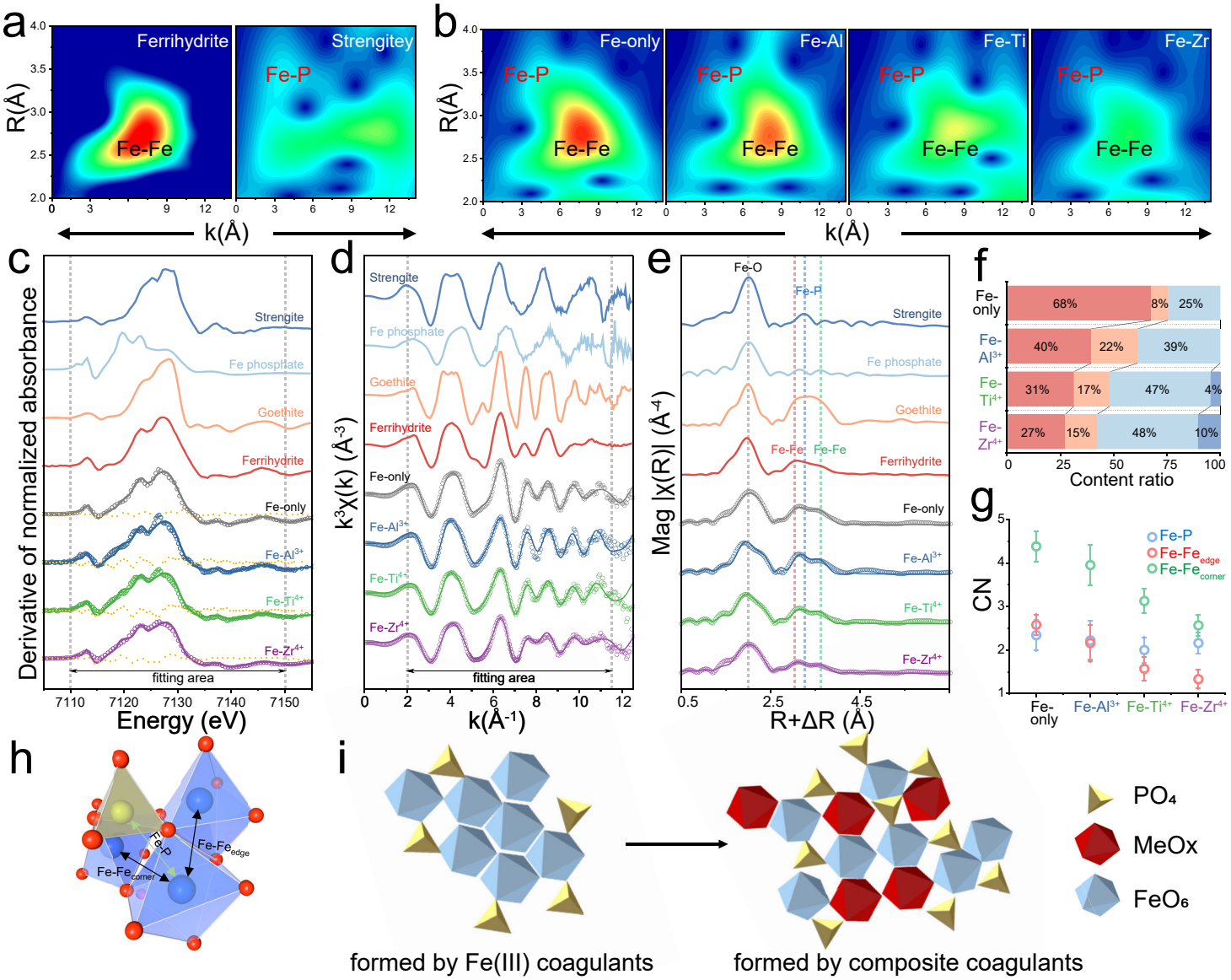


Figure 5. The EXAFS analysis of flocs is formed by different coagulants in AT water. Wavelet transformation signals of standard mineral (ferrihydrite and strengite) (a); Wavelet transformation signals of flocs formed by Fe(III) and composite coagulants (b); linear fitting results of the first derivative of Fe K-edge XANES spectra of mineral references and formed flocs (dashed lines represent the original data, solid lines represent fitting results, and the yellow dotted lines represent the fitting error) (c); shell fitting results of k^3 weighted EXAFS spectra (d) and Fourier-transform (FT) magnitude spectra (e) of mineral references and formed flocs (dashed lines represent the original data, solid lines represent fitted results); possible composition of formed flocs based on linear fitting (f); coordination number with the central Fe atom of different paths (h) calculated based on shell fitting (g); schematic diagram of structure differences between flocs formed by Fe(III) and composite coagulant (i).

Click here to access/download
Electronic Supplementary Material (for online publication only)
SI.pdf

Declaration of interests

✓The authors declare that they have no known competing financial interests or personal relationships that could have appeared to influence the work reported in this paper.

☐The authors declare the following financial interests/personal relationships which may be considered as potential competing interests: